

SELF-CONSISTENT MHD MODELING OF A CORONAL MASS EJECTION, CORONAL DIMMING, AND A GIANT CUSP-SHAPED ARCADE FORMATION

DAIKOU SHIOTA¹, HIROAKI ISOBE², P. F. CHEN³, TETSUYA T. YAMAMOTO⁴,
TAKUMA SAKAJIRI¹, AND KAZUNARI SHIBATA¹

ABSTRACT

We performed magnetohydrodynamic simulation of coronal mass ejections (CMEs) and associated giant arcade formations, and the results suggested new interpretations of observations of CMEs. We performed two cases of the simulation: with and without heat conduction. Comparing between the results of the two cases, we found that reconnection rate in the conductive case is a little higher than that in the adiabatic case and the temperature of the loop top is consistent with the theoretical value predicted by the Yokoyama-Shibata scaling law. The dynamical properties such as velocity and magnetic fields are similar in the two cases, whereas thermal properties such as temperature and density are very different. In both cases, slow shocks associated with magnetic reconnection propagate from the reconnection region along the magnetic field lines around the flux rope, and the shock fronts form spiral patterns. Just outside the slow shocks, the plasma density decreased a great deal. The soft X-ray images synthesized from the numerical results are compared with the soft X-ray images of a giant arcade observed with the Soft X-ray Telescope aboard *Yohkoh*, it is confirmed that the effect of heat conduction is significant for the detailed comparison between simulation and observation. The comparison between synthesized and observed soft X-ray images provides new interpretations of various features associated with CMEs and giant arcades. 1) It is likely that Y-shaped ejecting structure, observed in giant arcade 1992 January 24, corresponds to slow and fast shocks associated with magnetic reconnection. 2) Soft X-ray twin dimming

¹Kwasan and Hida Observatories, Kyoto University, Yamashina, Kyoto 607-8471 Japan; shiota@kwasan.kyoto-u.ac.jp

² Department of Earth and Planetary Science, University of Tokyo, Bunkyo-ku, Tokyo 113-0033, Japan

³Department of Astronomy, Nanjing University, Nanjing 210093, China

⁴Department of Astronomy, School of Science, University of Tokyo, Bunkyo-ku, 113-0033 Tokyo, Japan

corresponds to the rarefaction induced by reconnection. 3) The inner boundary of the dimming region corresponds to the slow shocks. 4) “Three-part structure” of a CME can be explained by our numerical results. 5) The numerical results also suggest a backbone feature of a flare/giant arcade may correspond to the fast shock formed by the collision of the downward reconnection outflow.

Subject headings: conduction — MHD — shock waves — Sun: corona

1. INTRODUCTION

Coronal mass ejections (CMEs) are one of the most spectacular phenomena in the solar corona. CMEs show some kind of association with various forms of solar activities; 40% of CMEs were associated with flares, but more than 70% were associated with eruptive prominence or disappearing filaments (Munro et al. 1979; Webb & Hundhausen 1987; see Kahler 1992 for review). On the other hand, observations with Soft X-ray Telescope (SXT) aboard *Yohkoh* revealed that formations of giant arcades are associated with filament eruptions that are not associated with flares (Tsuneta et al. 1992; Hiei et al. 1993, Hanaoka et al. 1994; McAllister et al. 1996). Although such arcades are usually not recognized as flares because of their weak X-ray intensity, they have arcade structures with expanding cusp-shaped loops (helmet streamer), which is very similar to flares. From this and other evidence (e.g. Yamamoto et al. 2002) it has been argued that their mechanism is the same as that of flares; magnetic reconnection. Considering these observations, Shibata (1996; 1999) suggest that CMEs, filament eruptions, flares/giant arcades can be understood in a unified view: mass ejection and magnetic energy release via magnetic reconnection (Fig. 1).

Although each CME shows different, complex structure, many of them have a typical structure, so called “three-part structure”, which consists of a bright core, a surrounding cavity, and a slightly bright outer edge (Illing & Hundhausen 1985). A prominence surrounded by dark cavity is often observed inside a helmet streamer in the pre-eruption stage, and this structure appears to swell once an eruption starts. This scenario is thought to be a simple interpretation of the formation of a three-part CME (see Hundhausen 1999 for review). On the other hand, Lin et al. (2004) developed a semi-analytical reconnection model of a CME and explained three-part structure formation.

On the other hand, *coronal dimmings* explained as the EUV or SXR decrease, are often observed around post-erupting loops (Sterling & Hudson 1997; Zarro et al. 1999). The observation with Coronal Diagnostic Spectrometer (CDS) aboard Solar and Heliospheric Observatory (SOHO) showed that dimming was caused not by the decrease in temperature

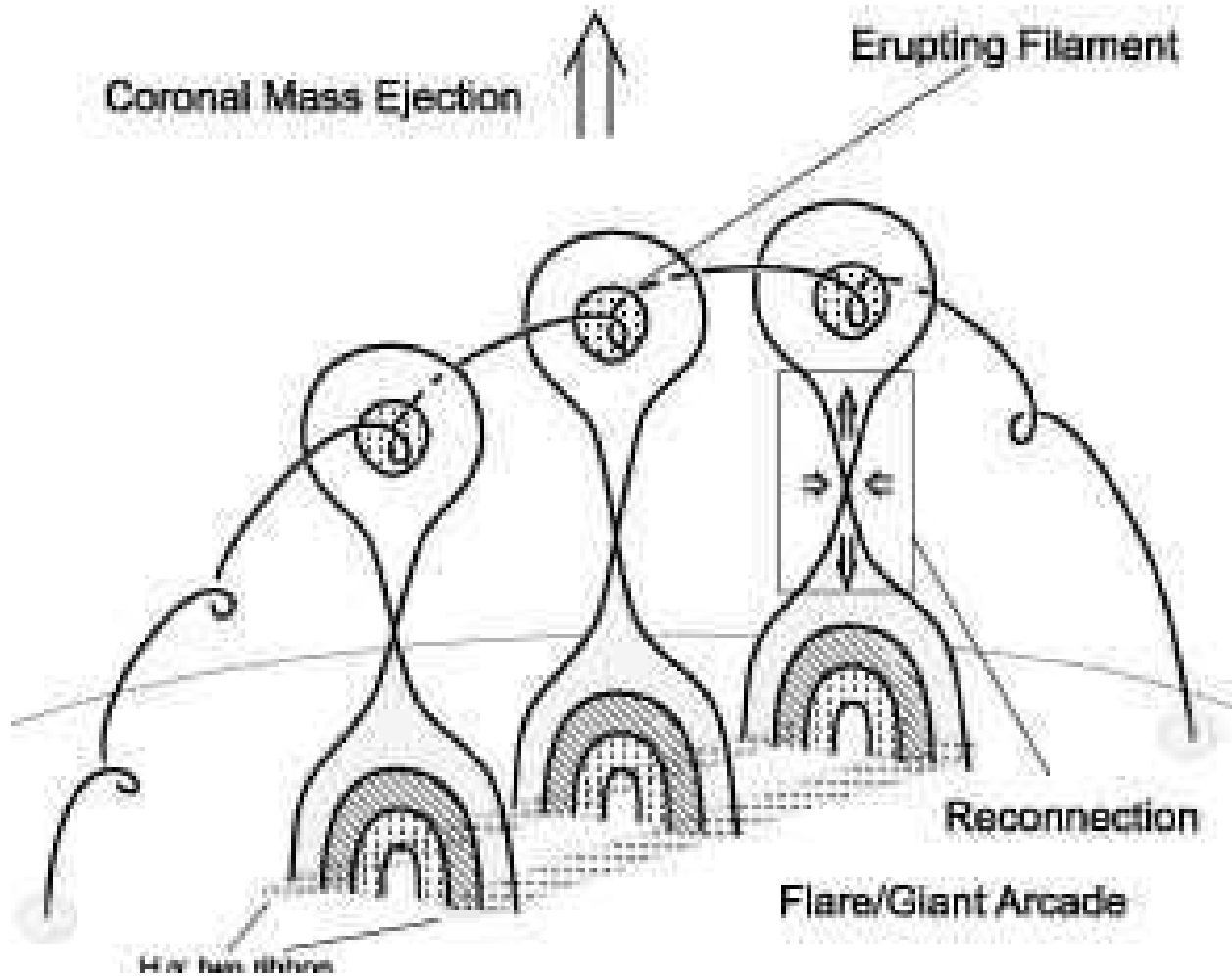


Fig. 1.— Schematic picture of the standard model of the phenomenon observed as a CME and a flare/giant arcade. Thick solid lines show magnetic field lines. Note that the points where magnetic field lines cross are the X-type neutral points where magnetic reconnection occurs. Gray-shaded, line-shaded, and dot-shaded regions display the features observed in soft X-ray, extreme ultraviolet ray, and $H\alpha$, respectively.

but by the decrease in plasma density (Harrison & Lyons 2000). This results indicate that the mass which existed there in the pre-eruption stage are lost. Furthermore, Harra & Sterling (2001) showed blue-shifted motion coincided with coronal dimming in the CDS observations, and therefore, suggested the lost mass is supplied to the CME. On the other hand, reconnection inflow can rarefy the inflow region (Tsuneta 1996, Nitta et al. 2001). It remains unclear which mechanism causes the dimmings.

In this paper we propose a new model that explains the formation of the three-part structure of CMEs and the mechanism of dimmings self-consistently. We performed 2.5-dimensional magnetohydrodynamic (MHD) simulations of a coronal mass ejection associated with a giant cusp-shaped arcade, where 2.5-D means that three vector components are included but the space is two dimension. The numerical results are compared with the observations of CMEs and associated phenomena in order to clarify their evolution processes.

Before describing the numerical model in detail, it would be better to discuss the situation of the problem. In solar flares, magnetic energy is thought to be converted into kinetic and thermal energies by magnetic reconnection. In the corona, because the thermal conductivity is very high, thermal energy is conducted very rapidly along the field lines. When the conducted thermal energy heats the dense chromospheric plasma (or nonthermal electrons collide to chromospheric plasma), the gas pressure increases suddenly. The pressure gradient generates upward flow to the corona, and the flare loop is filled by the plasma comes from the chromosphere. This process is called as chromospheric evaporation (Hirayama 1974). The flare loops filled by the hot dense plasma loses energy by radiation.

There are three key physical processes for energy balance: conduction, radiation, and reconnection. The time scales of conductive cooling, radiative cooling, and reconnection heating are

$$t_{\text{cond}} \equiv \frac{3nk_{\text{B}}L^2}{\kappa_0 T^{5/2}}, \quad (1)$$

$$t_{\text{rad}} \equiv \frac{3nk_{\text{B}}T}{n^2 Q(T)}, \quad (2)$$

and

$$t_{\text{rec}} \equiv \frac{3nk_{\text{B}}T}{B^2/4\pi} \frac{L}{v_{\text{A}}} \quad (3)$$

respectively, where k_{B} is the Boltzmann constant, $\kappa_0 (= 10^{-6}$ CGS) is heat conduction coefficient along magnetic field (Spitzer 1962), $Q(T)$ is the radiative loss function (Raymond, et al. 1976). The time scale of reconnection heating is derived from Poynting flux of inflow region. In the condition of giant arcade in quiet region ($n = n_0 = 2 \times 10^8 \text{ cm}^{-3}$, $T = T_0 = 2 \times 10^6$ K, $L = L_0 = 2 \times 10^{10}$ cm, $B = 3$ G, $v_{\text{A}} = B/\sqrt{4\pi\rho} \sim 4.7 \times 10^7 \text{ cm s}^{-1}$, and $Q(T) \sim 10^{-22} \text{ erg cm}^3 \text{ s}^{-1}$; Yamamoto et al. 2002), $t_{\text{cond}} \sim 3 \times 10^3$ sec, $t_{\text{rad}} \sim 4 \times 10^4$ sec, and $t_{\text{rec}} \sim 97$

sec. Since t_{rad} is much longer than t_{rec} , we can neglect the effect of radiative cooling for this reconnection problem. Though t_{cond} is also longer than t_{rec} at the initial state, the effect of conduction cannot be neglected because the temperature increases due to reconnection heating, so that t_{cond} becomes comparable to or even shorter than t_{rec} .

Although magnetic reconnection coupled with heat conduction is important for solar flares, MHD simulations for such a problem are performed by only few researchers because of its numerical difficulty (Yokoyama & Shibata, 1997,1998, 2001, Chen et al. 1999). These authors adopted antiparallel field for initial magnetic configuration. For the comparison with observations, however, we have to perform simulations in more realistic conditions. In our simulation, we adopted initial magnetic field configuration of Chen and Shibata (2000) and include the effect of heat conduction and discuss what difference the effect makes. The initial results of this study have already been published in Shiota et al. (2003).

In the next section, the numerical method is described. The numerical results are shown and the differences between adiabatic and conductive cases are described in §3. The numerical results of the conductive case are compared with *Yohkoh* observations in §4. Finally, summary and discussions are given in §5.

2. NUMERICAL MODELS

2.1. Numerical Method

We perform simulations with a multi-step implicit scheme (Hu 1989) for two cases: a case without heat conduction (case A) and a case with heat conduction (case B). Two-and-a-half dimensional time-dependent resistive MHD equations considered in this study are as follows:

$$\frac{\partial \rho}{\partial t} + \nabla \cdot (\rho \mathbf{v}) = 0, \quad (4)$$

$$\frac{\partial \mathbf{v}}{\partial t} + (\mathbf{v} \cdot \nabla) \mathbf{v} + \frac{1}{\rho} \nabla P - \frac{2}{\beta_0} \frac{1}{\rho} \mathbf{j} \times \mathbf{B} = 0, \quad (5)$$

$$\frac{\partial \mathbf{B}}{\partial t} - \nabla \times (\mathbf{v} \times \mathbf{B}) + \nabla \times (\eta \nabla \times \mathbf{B}) = 0, \quad (6)$$

$$\frac{\partial T}{\partial t} + \mathbf{v} \cdot \nabla T + (\gamma - 1) T \nabla \cdot \mathbf{v} - \frac{2(\gamma - 1)\eta}{\rho \beta_0} \mathbf{j} \cdot \mathbf{j} - C \frac{1}{\rho} Q = 0, \quad (7)$$

where $\mathbf{B} = \nabla \times (\psi \hat{\mathbf{e}}_z) + B_z \hat{\mathbf{e}}_z$, $\mathbf{j} = \nabla \times \mathbf{B}$, η is magnetic resistivity, the quantity Q and C are the dimensionless heat conduction function and its coefficient. The seven independent variables are the plasma density (ρ), temperature (T), velocity (v_x, v_y, v_z), magnetic flux

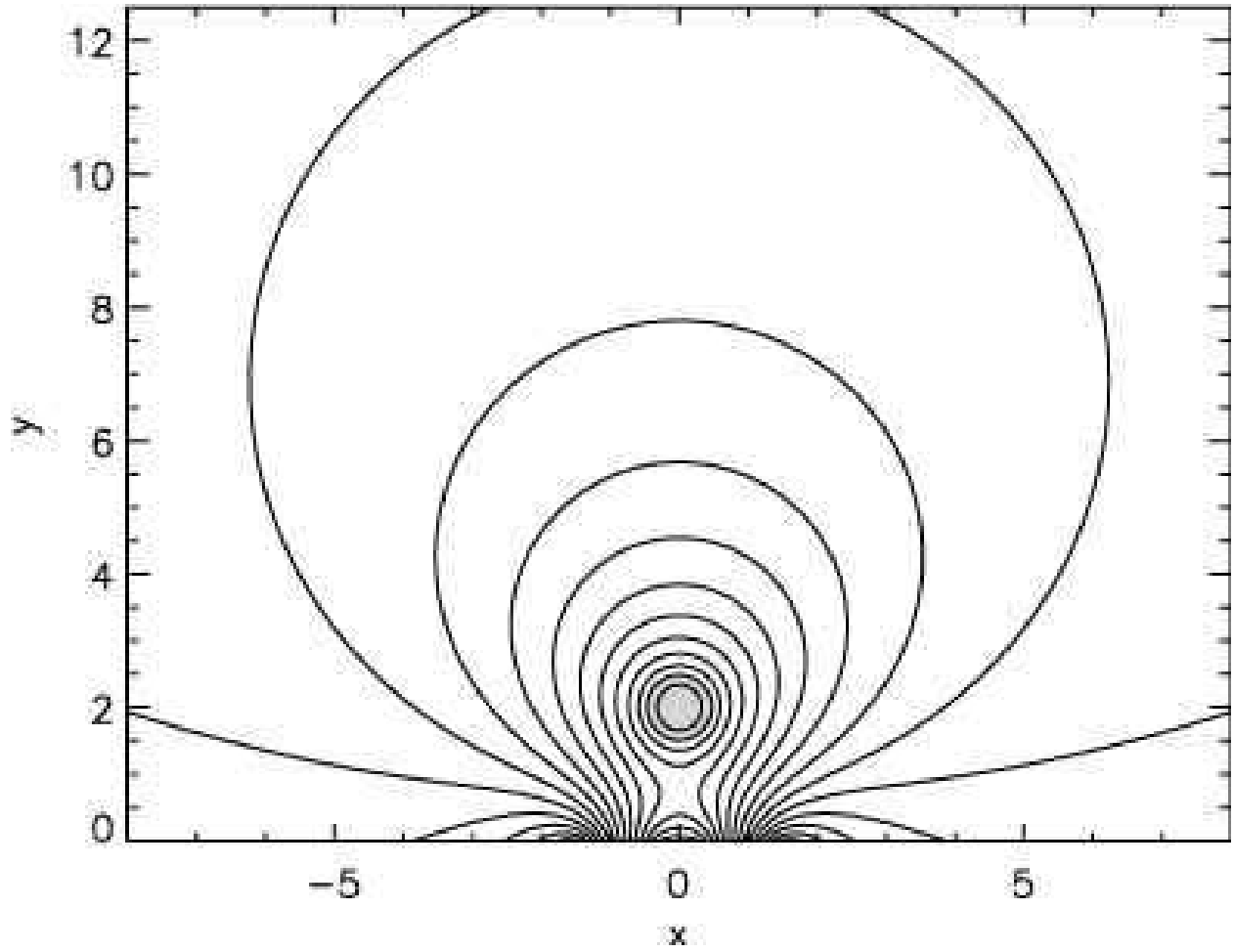


Fig. 2.— Initial magnetic field configuration. Solid lines show magnetic field lines. the position of the flux rope is displayed by gray shadow.

function (ψ), and perpendicular component of magnetic field (B_z). The seven variables normalized with the characteristic values of giant arcades are used in the equations (4) - (7). The characteristic values of length, density, and temperature are obtained from the Yohkoh observations (see Yamamoto et al. 2002), which are $L_0 = 2 \times 10^{10}$ cm, $\rho_0 = 3.2 \times 10^{-16}$ g cm $^{-3}$ (i.e., $n_0 = 2 \times 10^8$ cm $^{-3}$), and $T_0 = 2 \times 10^6$ K, respectively. The unit of velocity is

$$v_0 = C_s = \sqrt{\frac{2k_B T_0}{m_H}} = 181.8 \text{ km s}^{-1}, \quad (8)$$

where k_B is Boltzmann constant and m_H is the mass of hydrogen atom. The unit of magnetic field strength is chosen as

$$B_0 = \sqrt{\frac{16\pi\rho_0 k_B T_0}{m_H \beta_0}} = 16.66 \text{ G}. \quad (9)$$

The parameter β_0 is the ratio of gas to magnetic pressure at the surface of the flux rope (magnetic configuration is described in next subsection). β_0 is chosen to be 0.01. The unit of time becomes $\tau_{A0} = L_0/v_{A0}$, where v_{A0} is the local Alfvén velocity around the flux rope ($v_{A0} = B_0/\sqrt{4\pi\rho_0} = 2571$ km s $^{-1}$) and $\tau_{A0} = 77.8$ s.

In only case B, we assume anisotropic Spitzer type heat conduction, Q and C in equation (7) are written as follows:

$$Q = \begin{cases} 0, & \text{(caseA)} \\ \nabla \cdot \left(\kappa_0 T^{\frac{5}{2}} \frac{(\mathbf{B} \cdot \nabla T)}{\mathbf{B}^2} \mathbf{B} \right), & \text{(caseB)} \end{cases} \quad (10)$$

$$C = \frac{2(\gamma - 1)\kappa_0 T_0^{\frac{7}{2}}}{\rho_0 L_0 v_0^3}, \quad (11)$$

The resistivity(η) is taken as an anomalous type as follows:

$$\eta = \begin{cases} \eta_0 \left| \frac{v_d}{v_c} \right| - 1, & |v_d| \geq v_c, \\ 0, & |v_d| < v_c, \end{cases} \quad (12)$$

where $v_d \equiv j_z/\rho$ is the (relative ion-electron) drift velocity, and the dimensionless parameters are assumed as $v_c = 2.0$, and $\eta_0 = 0.002$. It is known that the anomalous resistivity may be caused by plasma instabilities (Coppi & Friedland 1971) in localized region, and localized resistivity triggers fast reconnection (Ugai & Tsuda, 1977).

The simulation box ($-8 \leq x \leq 8$, $0 \leq y \leq 12.5$) is discretized by 321×501 grid points, which are distributed non-uniformly in the x -direction and uniformly in the y -direction. The left ($x = -8$), the right ($x = 8$), and the upper boundaries ($y = 12.5$) are free boundaries

where the plasma, magnetic field, and waves could pass through freely. The bottom of the simulation box is a line-tying boundary where all quantities, except for T , are fixed outside of the emerging flux region (described in section 2.3). T is determined by extrapolation, i.e., the value was specified to be the same as that at its neighboring point.

2.2. Initial Condition

Initial magnetic field configuration is shown in Figure 2. We adopt this configuration to mimic a cross section of the arcade and the flux rope shown in Figure 1.

This configuration is presented by three separate current elements (see Chen & Shibata 2000): a line current contained within flux rope (which determines ψ_l), its image current below the photosphere (which determines ψ_i), and four line currents just below the photosphere (which determines ψ_b). Potential field created by those currents are expressed as follows:

$$\psi_b = \ln \frac{[(x + 0.3)^2 + (y + 0.3)^2][(x - 0.3)^2 + (y + 0.3)^2]}{[(x + 1.5)^2 + (y + 0.3)^2][(x - 1.5)^2 + (y + 0.3)^2]}, \quad (13)$$

$$\psi_i = -\frac{r_0}{2} \ln(x^2 + (y + h)^2), \quad (14)$$

$$\psi_l = \begin{cases} r^2/(2r_0), & r \leq r_0; \\ r_0/2 - r_0 \ln(r_0) + r_0 \ln(r), & r > r_0. \end{cases} \quad (15)$$

$$\psi = c\psi_b + \psi_l + \psi_i \quad (16)$$

where h is the height of the flux rope and r_0 is the radius of the flux rope, which determine the configuration of magnetic field. In this study, we set $h = 2.0$ and $r_0 = 0.5$. The coefficient c in the formula (16) represents the strength of background field. This is determined by trial and error in order to guarantee that the flux rope center approximately keeps stable for long enough time. In this study, it is set to be 0.2534. This physical meaning is as follows. If we remove the flux rope, the magnetic field configuration are potential quadrupole field, produced by the four line currents and the image current below the photosphere. This configuration makes a null point above the photosphere. If we set at the null point a flux rope whose radius is infinitesimal, the configuration is in unstable equilibrium. However in the simulation, the flux rope has a finite radius and therefore, we have to seek the solution very near to equilibrium.

To satisfy the force balance within the flux rope, a perpendicular magnetic component

(i.e., B_z) was introduced inside the flux rope:

$$B_z = \begin{cases} \sqrt{2(1 - \frac{r^2}{r_0^2})}, & r \leq r_0; \\ 0, & r > r_0, \end{cases} \quad (17)$$

Other quantities are set to be uniform; $(\rho, T, v_x, v_y, v_z) = (1.0, 1.0, 0.0, 0.0, 0.0)$.

2.3. CME Triggering mechanism

Statistical studies by Feynman & Martin (1995) show that reconnection favorable emerging flux is correlated well with CMEs. The meaning of reconnection favorable is that the orientation of newly emerging flux is opposite to that of pre-existing large scale coronal magnetic field. With numerical simulations, Chen & Shibata (2000) confirmed the discovery of Feynman & Martin (1995) that such emerging flux can trigger a CME.

In this study, we adopt one case of Chen-Shibata model, in which newly emerging flux appears just below the flux rope. The emerging process was realized by changing the magnetic field at the bottom boundary within $-0.2 \leq x \leq 0.2$.

3. NUMERICAL RESULTS

Time evolutions of density and temperature distributions in cases A and B are shown in Figures 3 and 4, respectively.

The dynamical evolutions of both cases are almost the same as that of case A in Chen & Shibata (2000). Magnetic reconnection occurs between the newly emerged flux and magnetic field just above it, which leads to partial magnetic cancellation, and hence the decrease in magnetic pressure. The magnetized plasma at both sides (left and right to the magnetic null point [X point]) moves inward. Then magnetic field lines at both sides are pushed in, and therefore a current sheet is formed near the X point. The current density inside of the sheet increases nearly exponentially. When the condition equation (12) is satisfied, anomalous resistivity sets in and fast reconnection occurs. The upward outflow associated with reconnection pushes the flux rope up.

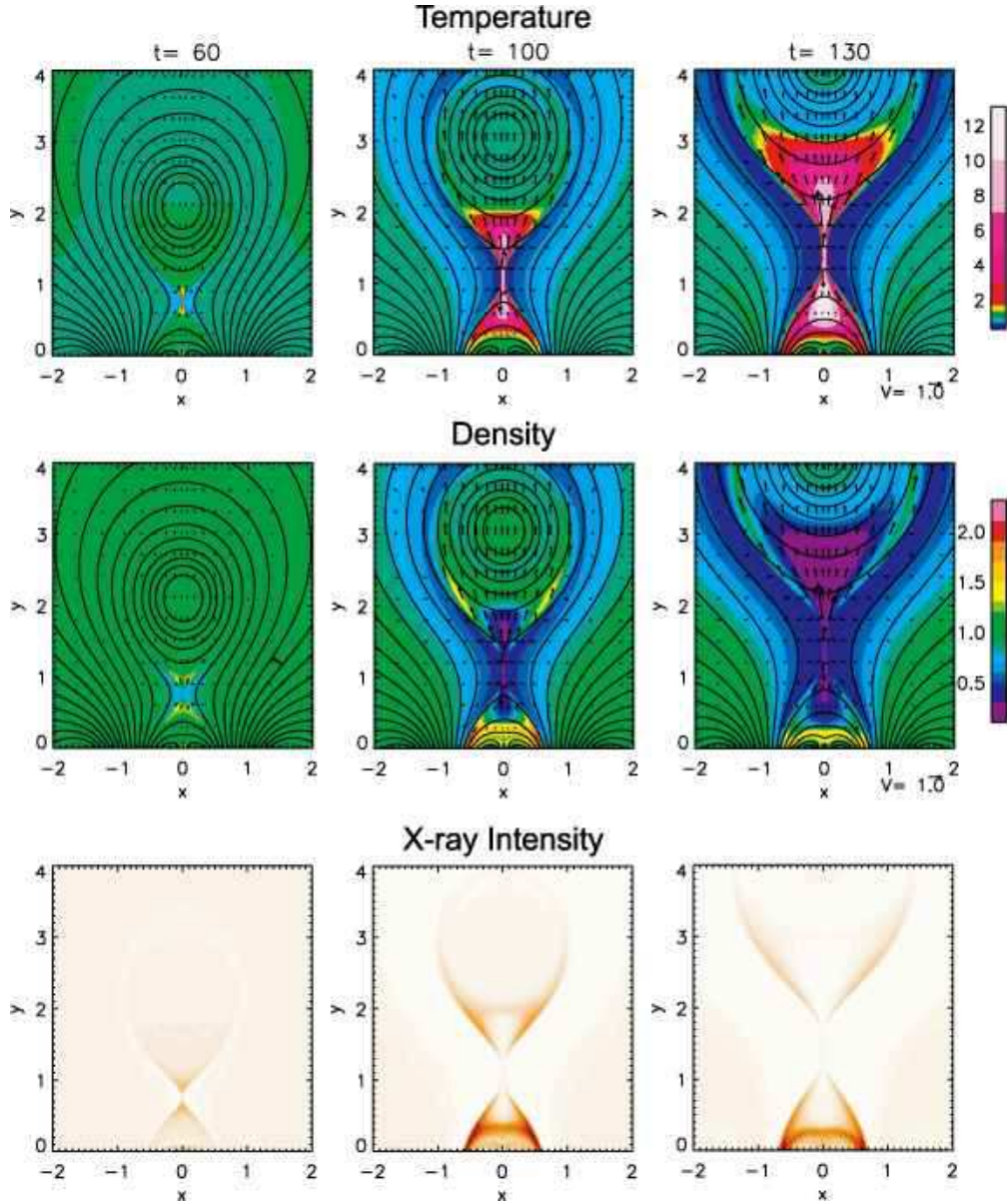


Fig. 3.— Numerical results of case A. Upper panels are temperature distributions at $t = 60$, 100, and 130. Middle panels are density distributions at same times as upper ones. Colors display the quantities. Arrows shows velocity field at the points and solid lines show magnetic field lines. Lower panels are X-ray intensity distributions at same times. The X-ray intensity are calculated from the numerical results after taking account of the filter response function of the Yohkoh/SXT. The normalization units are $\tau_{A0} = 77.8$ s, $L_0 = 2 \times 10^{10}$ cm, $n_0 = 2 \times 10^8$ cm $^{-3}$, and $T_0 = 2 \times 10^6$ K. The times $t = 60$, 100, and 130 mean 78, 130, and 169 minutes from the start of the simulation.

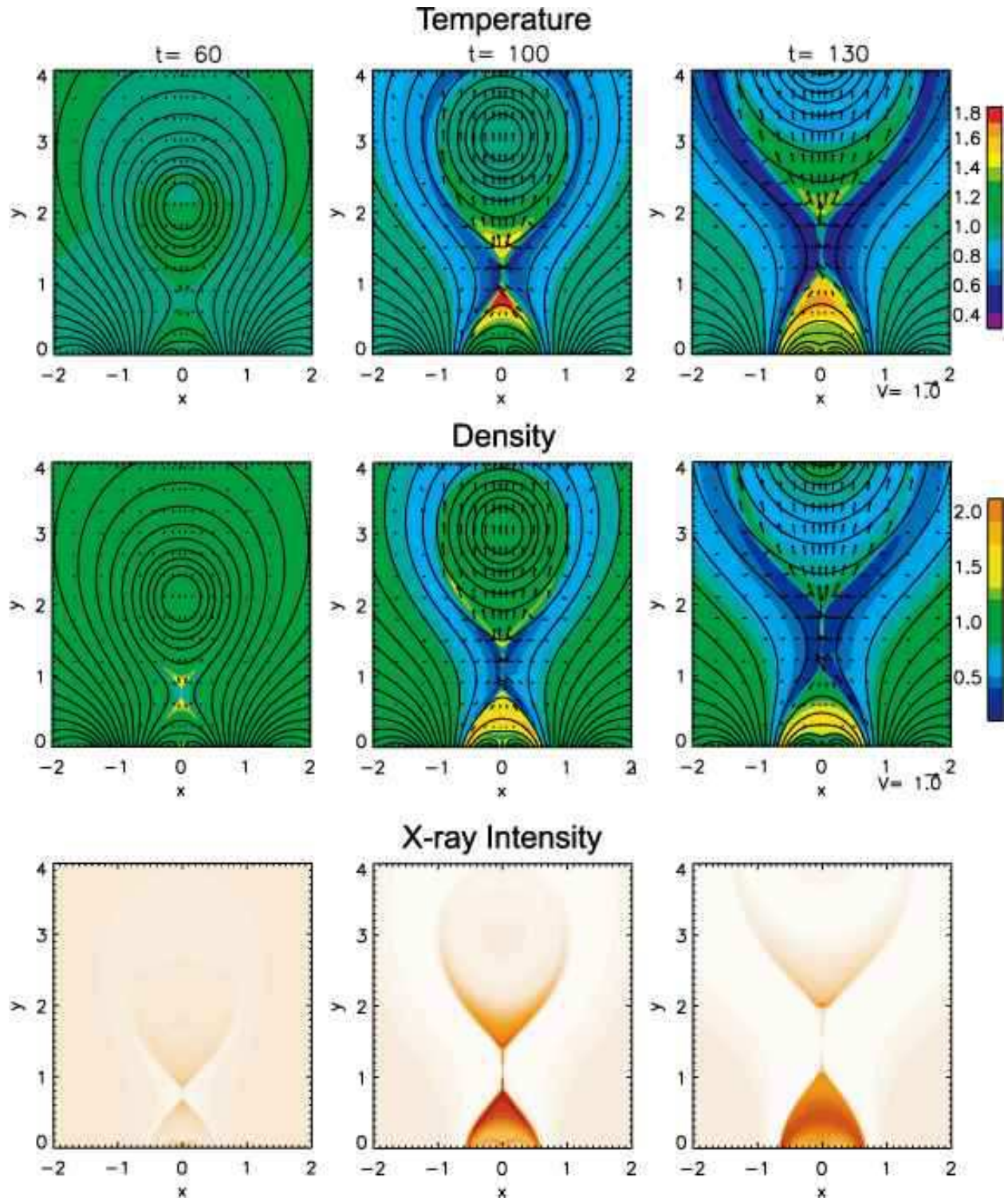


Fig. 4.— Numerical results of case B. Temperature, density and X-ray intensity distributions are displayed with same way as Figure 3.

3.1. Effect of Heat Conduction

The clearest difference between two cases is the difference in density and temperature distributions within the reconnection outflows (see Figures 3 and 4). In both cases, the plasma that passes through the reconnection region (the X point) is heated very much by Joule heating. However, in case B, because the heat conduction function become much larger in high temperature region, the heat is conducted along the field lines. Therefore, the temperature in reconnection region and within the reconnection outflows in case B becomes lower than that in case A. The gas pressure at the reconnection region balances with the gas and magnetic pressure outside the current sheet. Magnetic field strength and gas pressure at outside of the current sheet are almost the same in both cases. Therefore, plasma density at reconnection region in case B become higher.

It is found that global dynamics of the two cases are almost the same. Figure 5(a) shows trajectories of the flux ropes and the X points, and Figure 5(b) shows reconnection rates, in both cases. A little difference of dynamics is caused by the difference in the time evolutions of reconnection rate. Reconnection rate is defined as the reconnected magnetic flux per unit time and equals to the electric field \mathbf{E} in the diffusion region, i.e.,

$$\frac{d\psi_{\text{Xpoint}}}{dt} = \mathbf{E} \sim \mathbf{v}_{\text{in}} \times \mathbf{B}_{\text{in}} \sim \eta j_{\text{Xpoint}} \sim \eta \frac{\mathbf{B}_{\text{in}}}{d} \quad (18)$$

where ψ_{Xpoint} and j_{Xpoint} are magnetic flux function and current density at the X point, respectively, \mathbf{v}_{in} and \mathbf{B}_{in} are velocity and magnetic field of inflow region, respectively, and d is the width of the current sheet. The reconnection rate in case A saturated earlier than in case B. Why reconnection rate in case A lower than in case B? Current density distribution at $t = 100$ in both case are displayed in Figure 6 . It is found that the current density at the X point in case B is larger than that in case A and the width of the current sheet in case B is thinner than that in case A. The reason is as follows: In the diffusion region, plasma is heated by magnetic energy dissipation, and gas pressure are increased there. The enhanced gas pressure balances the magnetic pressure in the inflow region. In case B, the heat of the inside plasma is conducted along the field lines, and therefore the inside pressure becomes less than that in case A. As the sheet is pressed more and more, the magnetic dissipation (plasma heating) becomes larger, and then the gas pressure balances magnetic pressure in the outside region. In other words, the compressibility is enhanced in case B. This is the reason why the reconnection is faster in case B. This results are consistent with Sato et al. (1990), Magara et al. (1996) and Chen et al. (1999).

Yokoyama & Shibata (1998, 2001) performed MHD simulation each of magnetic reconnection coupled with heat conduction. Considering the energy balance between the conduction cooling and the reconnection heating, they derived a temperature scaling law of the top

of a flare loop;

$$T_{\text{top}} \sim \left(\frac{B^3 L}{2\pi\kappa_0\sqrt{4\pi\rho}} \right)^{2/7} \quad (19)$$

where B and ρ are magnetic field strength and density in the inflow region, and L is the half length of the loop which is comparable to the height of the X point. We applied the scaling law to our numerical results. However, in our simulation non-uniform magnetic field is assumed for the initial condition, in contrast to that anti-parallel uniform magnetic field is used in Yokoyama-Shibata’s numerical simulation. It is not easy to define a typical value of magnetic field strength here, so we take the average one in the inflow region. Because of non-uniform magnetic field, the average magnetic field strength depends on the area we choose as the inflow region. We chose several cases (cases a, b, and c, as shown in Figure 7c) of the definition of the inflow regions. We tabulate the results for the definition of the inflow regions in Table 1. The values \bar{B} and $\bar{\rho}$ in Table 1 are the averages of magnetic field and density in each inflow region on the side of the X point $y = 1.075$ at $t = 100$ (Fig. 7). Using these values we calculate the theoretical temperature predicted by Yokoyama-Shibata’s scaling law. It is found that the temperatures predicted by Yokoyama-Shibata’s scaling law are roughly consistent with our results. The temperature of the loop tops may be determined by the condition just outside of the X point.

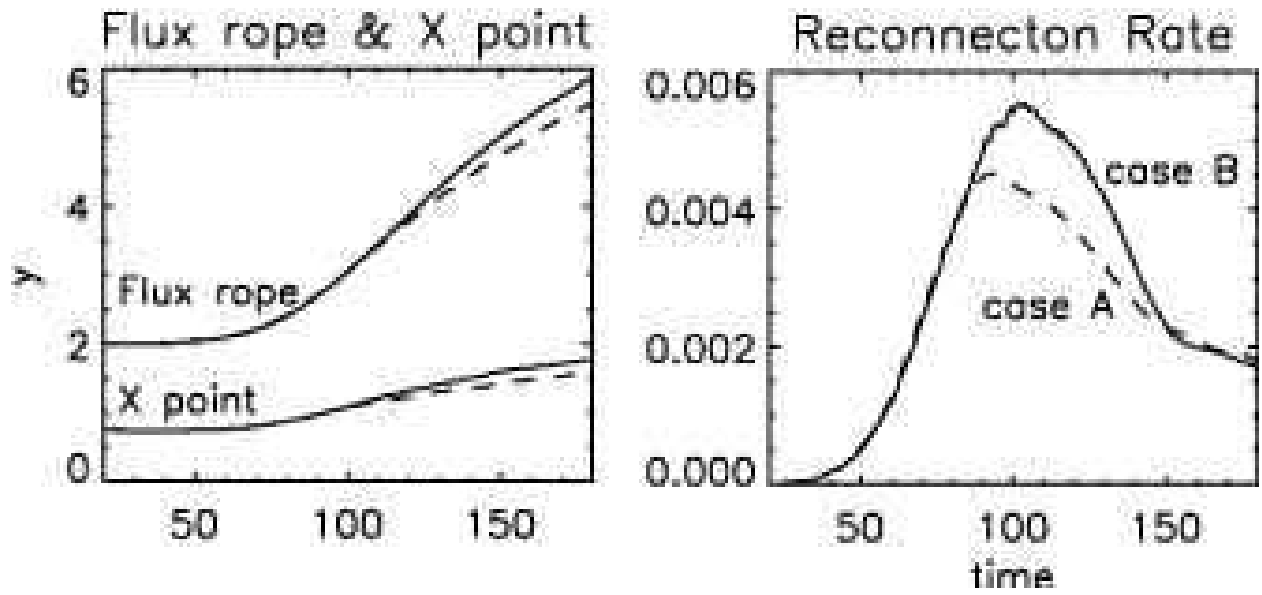


Fig. 5.— Left panel shows trajectories of center of flux rope and X point in both cases. Right panel shows reconnection rate in both cases. Solid lines are values in case B, dashed lines are in case A.

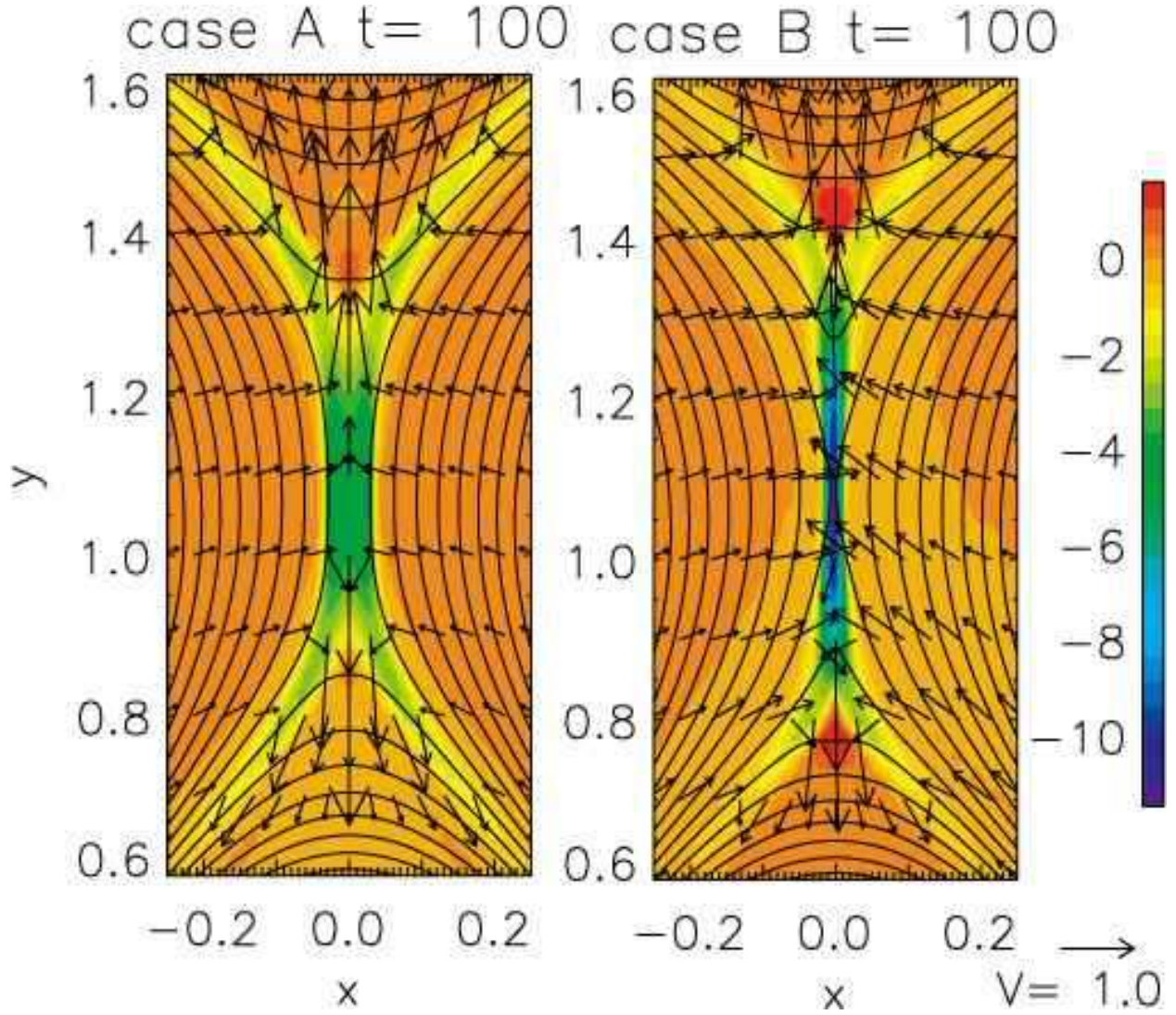


Fig. 6.— Structures around the X points at $t = 100$ in both cases. Gray scales show current density distributions. Arrows shows velocity field at the points and solid lines show magnetic field lines.

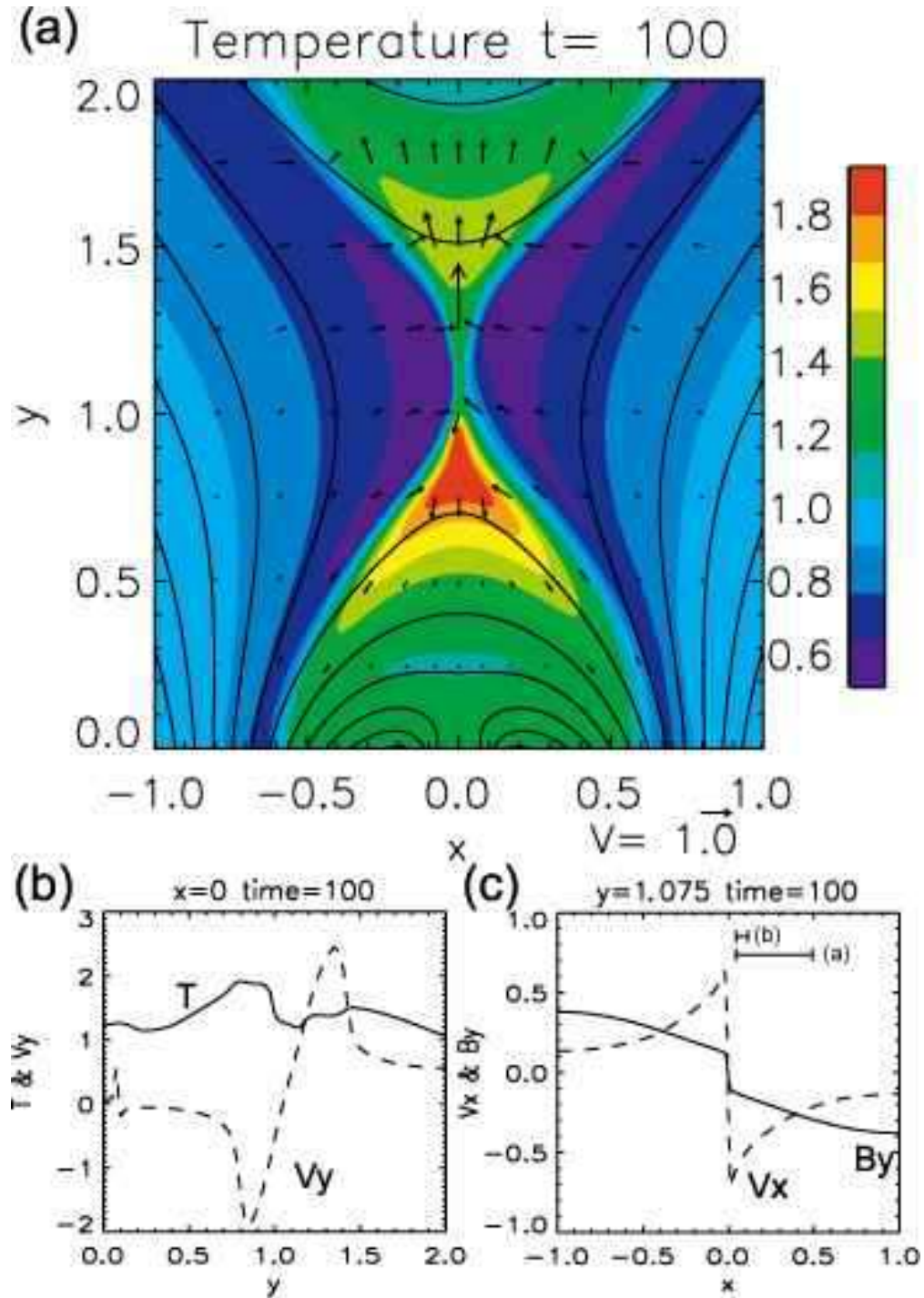


Fig. 7.— (a) temperature distribution at $t = 100$ in case B. (b) y -component of velocity (dashed lines) and temperature (solid line) along the y -axis at $t = 100$ in case B. (c) x -component of velocity (dashed lines) and y -component of magnetic field (solid line) along the line of $y = 1.075$ at $t = 100$ in case B.

Table 1: Temperature derived from Yokoyama-Shibata scaling law

	Inflow region	Mag. field \bar{B} (Gauss)	Density $\bar{\rho}$ (g cm ⁻³)	Temperature T_{YS} (K)
(a)	$0.022 \leq x \leq 0.505$	3.52	1.75e-16	1.0e+07
(b)	$0.022 \leq x \leq 0.103$	2.25	1.59e-16	6.9e+06
(c) ¹	$x = 0.022$	1.93	1.32e-16	6.2e+06
	Temperature at $(x, y) = (0, 0.75)$ in our results			3.6e+06

¹(c) $x = 0.022$ is the just outside of the current sheet

3.2. Fast and Slow MHD Shocks

Figure 8 shows the time evolutions of density distribution and the trajectory of each magnetic field line at $x = 0$ (upper panel), and reconnection rate at the X-point and the velocity of the flux rope (lower panel) in case B. From the figures, we can find that the flux rope is accelerated as reconnection rate increases. After the reconnection rate saturates, the flux rope is decelerated gradually. They seem to be closely related. We can also find propagating density discontinuities in Figure 8, which are also present in case A. The highest one propagating very rapidly is the fast-mode MHD wave driven by the flux rope, which steepens to a fast shock. This correspond to the forward fast shock of a CME found in interplanetary observations. The lowest two discontinuities (labeled with FS), through which newly appeared field lines pass, are formed by the collisions of reconnection outflows to the flux rope and the cusp-shaped loop. They may correspond to a reverse shock just below a CME and a termination shock above the top of a flare loop.

What are the two discontinuities nearest to the center of the flux rope (labeled with SS) ? Figure 9 shows the time evolutions of plasma and current densities distributions in case B. Just after magnetic reconnection starts around $t = 30$, current enhanced layers are formed along the field lines from the X point (separatrixes). The layers correspond to plasma density discontinuities, which are formed by the decrease of the outside density. The layers become a Y and inversed Y shaped structures, as the flux rope rises. Plasma velocity changes very much at these layers. Therefore, we can identify that the layers are MHD shocks. In figure 10c, the distributions of several physical quantities are plotted (gas pressure, density, temperature, velocity, magnetic field) along the white line shown in figures 10a and b. From Rankine–Hugoniot relations for oblique MHD shocks, the relation between quantities ahead (subscript with 1) and behind (subscript with 2) of shocks are given as follows (Priest 1982):

$$\frac{v_{2\perp}}{v_{1\perp}} = X^{-1} \quad (20)$$

$$\frac{v_{2\parallel}}{v_{1\parallel}} = \frac{v_1^2 - v_{A1}^2}{v_1^2 - Xv_{A1}^2} \quad (21)$$

$$\frac{B_{2\perp}}{B_{1\perp}} = 1 \quad (22)$$

$$\frac{B_{2\parallel}}{B_{1\parallel}} = \frac{(v_1^2 - v_{A1}^2)X}{v_1^2 - Xv_{A1}^2} \quad (23)$$

$$\frac{p_2}{p_1} = X + \frac{(\gamma - 1)X(v_1^2 - v_2^2)}{2c_{s1}^2} \quad (24)$$

where $X = \rho_2/\rho_1$, $v_{A1} = B_1/\sqrt{4\pi\rho_1}$, and $c_{s1} = \sqrt{\gamma p_1/\rho_1}$. Assuming that the shadowed region (Fig. 10) is an MHD shock, we can get the values ahead of the discontinuity from the

numerical results from the theory (Table 2). However, we cannot apply the relation exactly because our results present non-steady and non-uniform conditions, while steady and uniform condition are considered in the shock theory. Because nonuniform magnetic field is assumed for the initial condition, magnetic field is stronger toward the flux rope and the direction of magnetic field changed gradually. This is the reason why $B_{1\perp} < B_{2\perp}$. Taking into account this, we conclude that the quantities ahead and behind the discontinuities in the numerical results are roughly consistent with the shock relations and these discontinuities correspond to slow-mode MHD shocks associated with reconnection.

Table 2: Physical quantities ahead and behind of the shock

	upstream (simulation)	downstream (theory)	downstream (simulation)
ρ	0.431	–	0.873
v_{\perp}	-0.349	-0.172	-0.187
v_{\parallel}	-2.21	-0.964	-0.957
B_{\perp}	-0.019	-0.019	-0.047
B_{\parallel}	-0.228	-0.202	-0.173
p	0.254	1.934	2.215

From Figures 9 and 11, it is found that these slow shocks continue to propagate around the flux rope, the shock fronts form spiral patterns (white and gray lines in Fig. 11). These slow shocks correspond to the two discontinuities nearest to the flux rope in Figure 8.

Why the slow shock structure around flux rope has not been found so far ? Most of reconnection studies until now adopted anti-parallel magnetic field for initial condition. Figure 12 is a schematic pictures of the results of the simulation. In the anti-parallel case, the results of reconnection forms slow shocks as shown in upper right panels of Figure 12. The slow shocks propagate along field (along the current sheet). On the other hands, in our numerical simulation, initially current sheet does not exist. The field above the flux rope are closed. Because the slow shock propagates along the closed field, the spiral patterns are formed.

3.3. Rarefaction Structure

We can see the region where the density decreases (rarefaction) around the flux rope and the cusp-shaped loop in both cases, just outside the slow shocks discussed above. Why does the rarefaction occur ?

In order to examine the motion of the plasma we calculate the divergence of the velocity at $t = 100$ (Fig. 13). Figure 13a shows $\text{div } v$ with gray scales where the white indicates divergence (expansion) and the black indicates the opposite (compression). In order to clarify the mass motion, the velocity is divided into two components which are parallel and perpendicular to the magnetic field, shown as follows,

$$\mathbf{v}_{\parallel} = \frac{\mathbf{B} \cdot \mathbf{v}}{B^2} \mathbf{B} \quad (25)$$

$$\mathbf{v}_{\perp} = \mathbf{v} - \mathbf{v}_{\parallel}. \quad (26)$$

We also calculate the divergence of the two components of the velocity (Fig. 13 b and c).

When fast reconnection starts, upward and downward directed reconnection outflows are generated. The upward one collides with the flux rope and compresses the magnetic field (region 1 displayed in Fig. 13b). Since this compression causes a magnetic pressure increase and leads to flow along the field lines. In fact, the region 1 shows divergence in Figure 13b. The magnetic pressure increase in region 1 pushes the flux rope up.

The rise motion of the flux rope compresses the magnetic loops above it, and leads to the magnetic pressure increase. In addition, because the magnetic field strength in the initial condition decreases as $\sim y^{-3}$, the magnetic pressure decreases very rapidly. As the

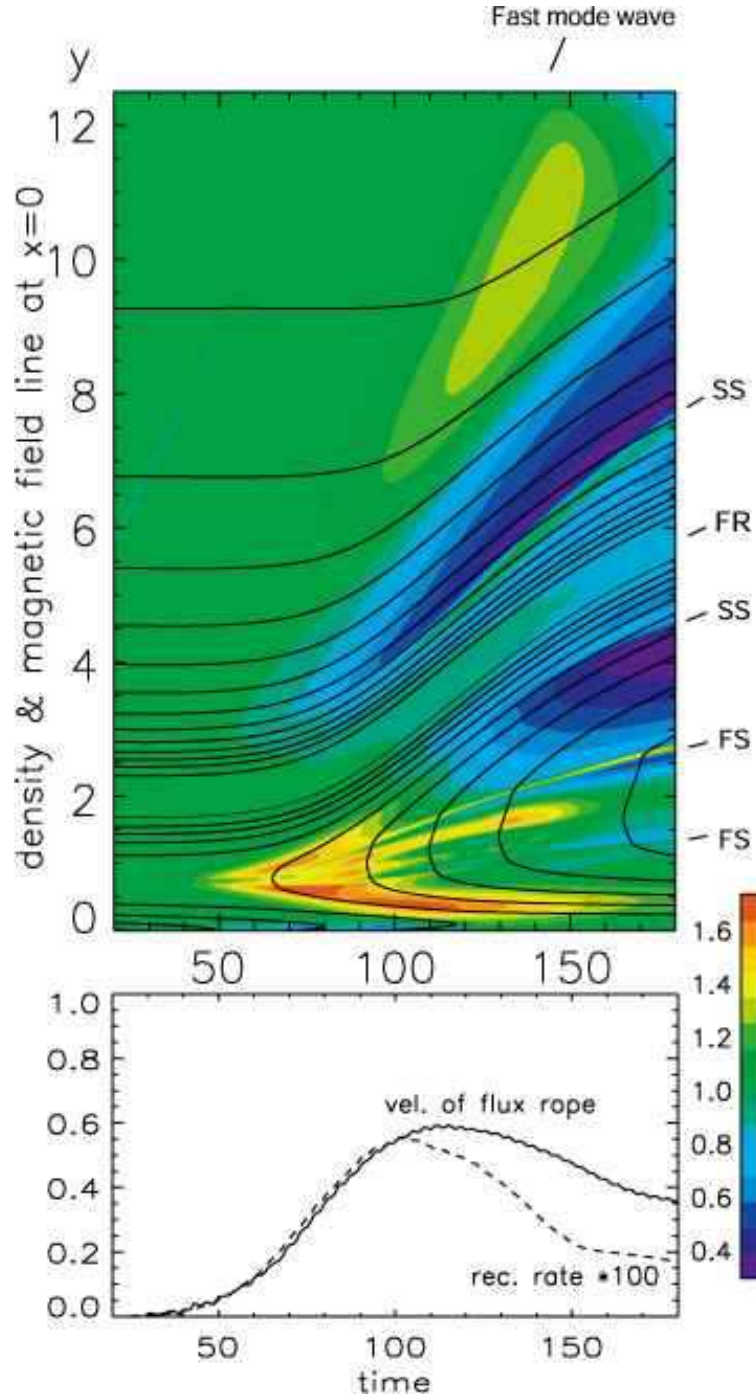


Fig. 8.— Time evolution of density at $x = 0$ in case B. Upper panel displays time evolution of density distribution at $x = 0$ with gray scales. Solid lines are trajectories of magnetic field lines. Lower panel shows reconnection rate and the velocity of the flux rope as function of time.

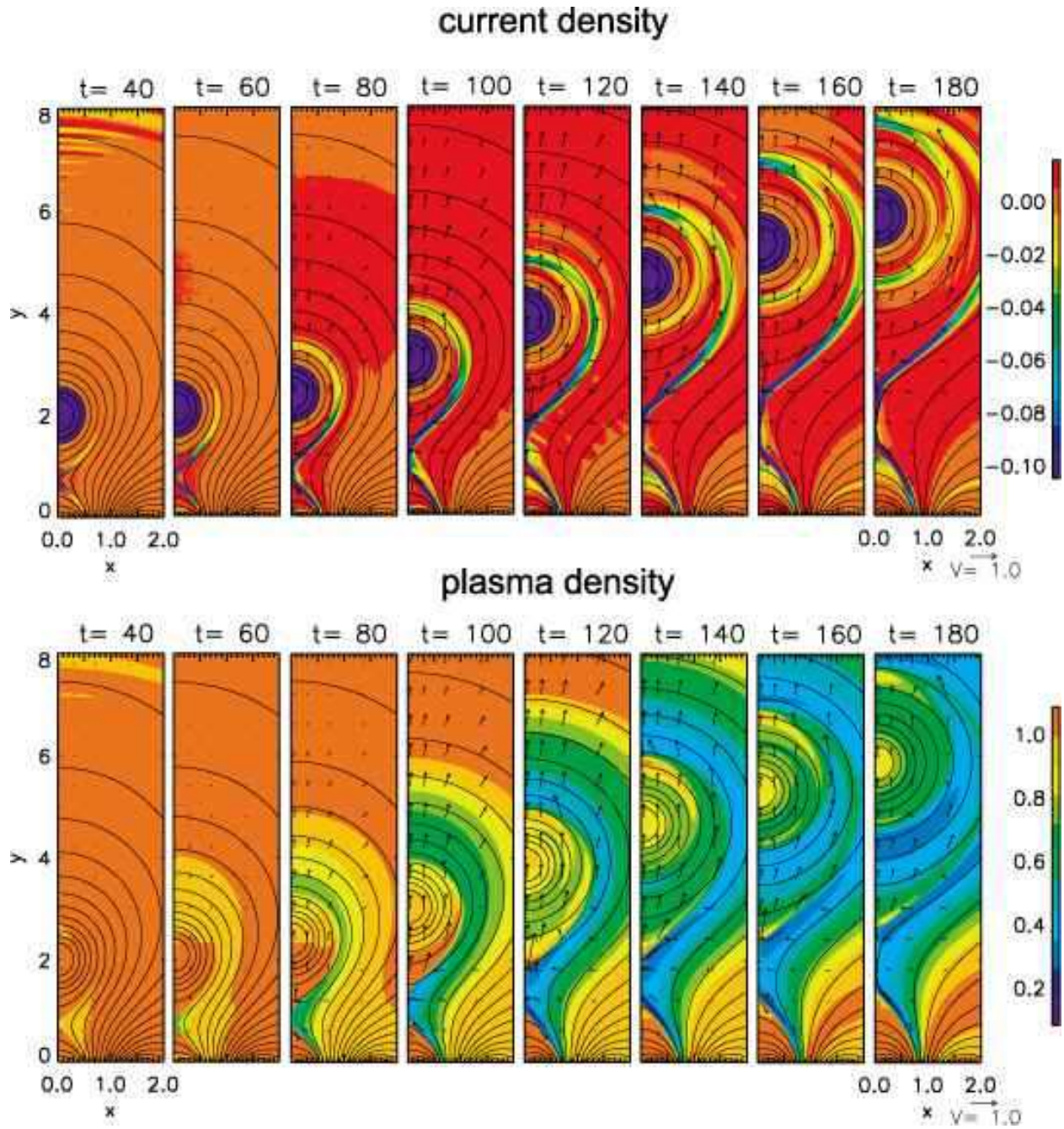


Fig. 9.— Time evolutions of plasma density and current density distributions. Colors show plasma density and current density, respectively. Arrows show velocity field at the points and solid lines show magnetic field lines.

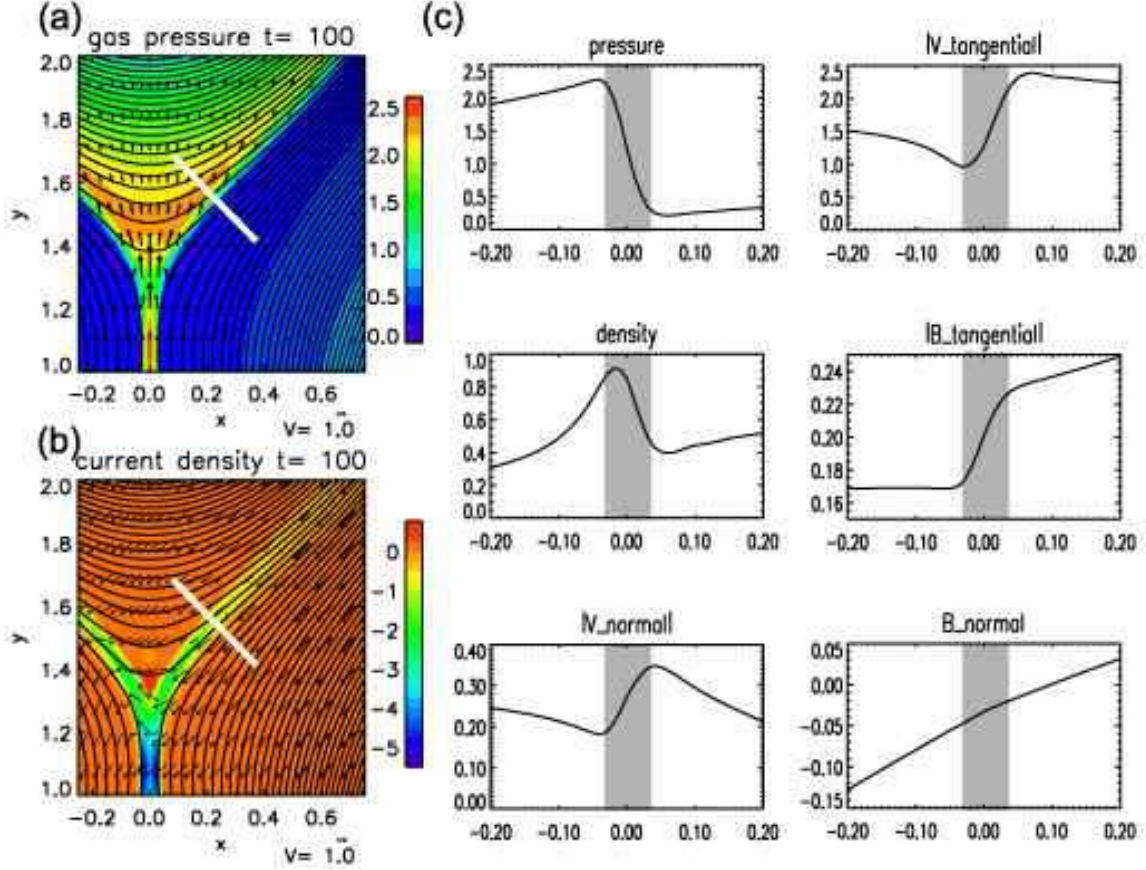


Fig. 10.— Physical quantities across the discontinuity. panels (a) and (b) are pressure and current density distributions at $t = 100$ in case A. Arrows show the velocity on the rest frame in panel (a) and velocity field on the shock front rest frame in panel (b). Panel(c) show gas pressure, density, tangential and normal components of velocity and magnetic field along the white line displayed in left panels.

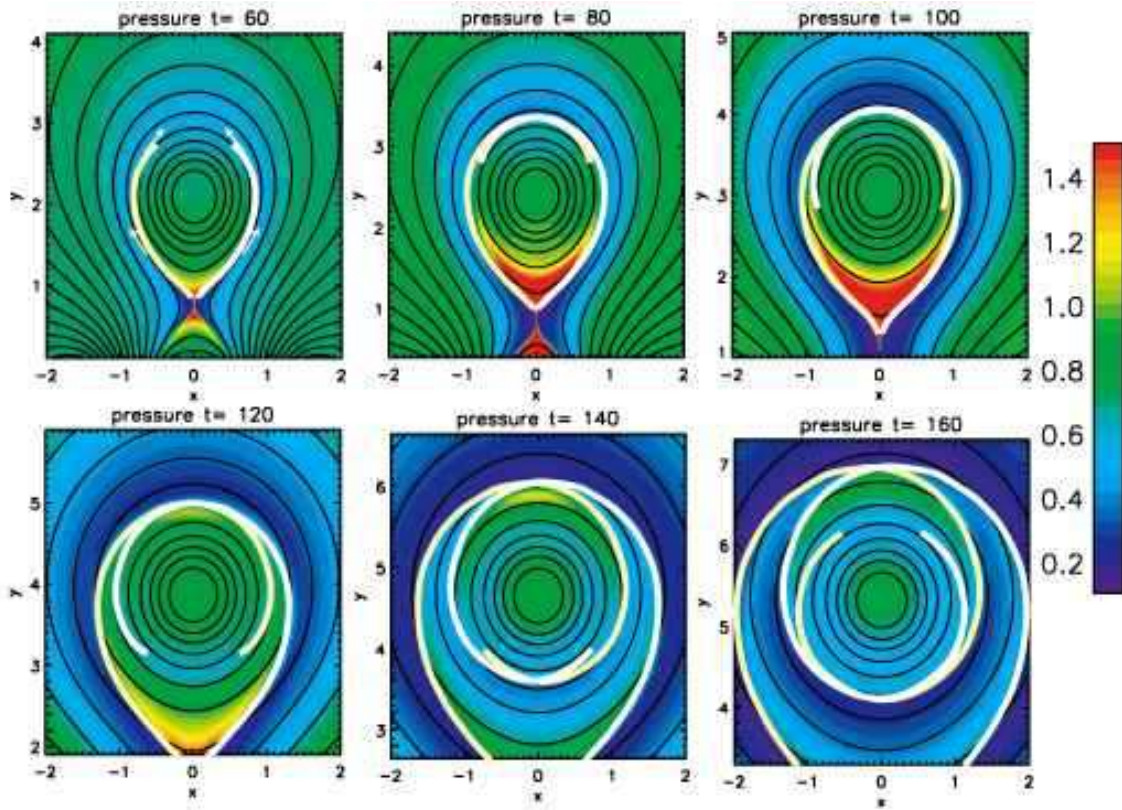


Fig. 11.— The time evolution of gas pressure around the flux rope. Colors show the gas pressure distributions. The centers of each panel are set to the center of the flux rope. White and yellow curves indicate the slow shock front and white arrows in the panel of $t = 60$ indicate the direction of the shock propagation.

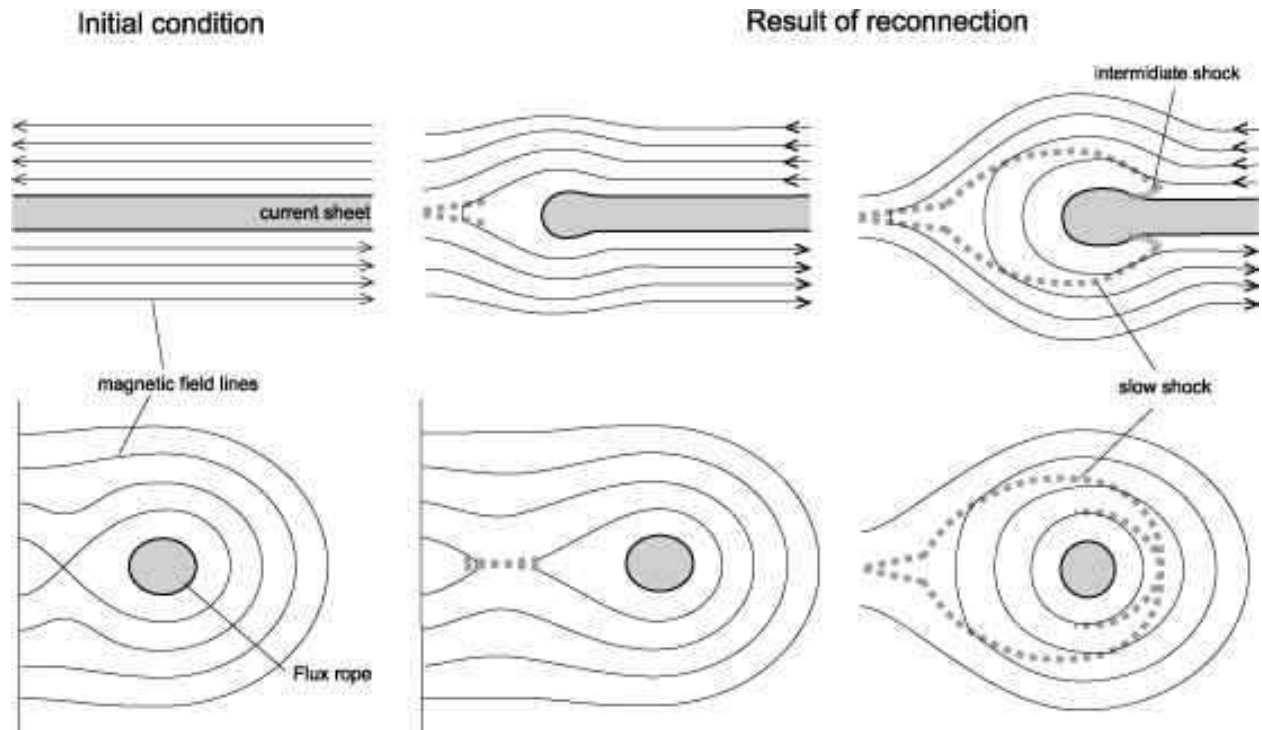


Fig. 12.— Schematic pictures of the results of magnetic reconnection in an anti-parallel field model and a flux rope model. In anti-parallel field model the slow shocks generated in reconnection region are terminated on intermediate shocks propagating along the current sheet. On the other hand, in flux rope model the current sheet does not exist, therefore, slow shocks generated in reconnection region are not terminated.

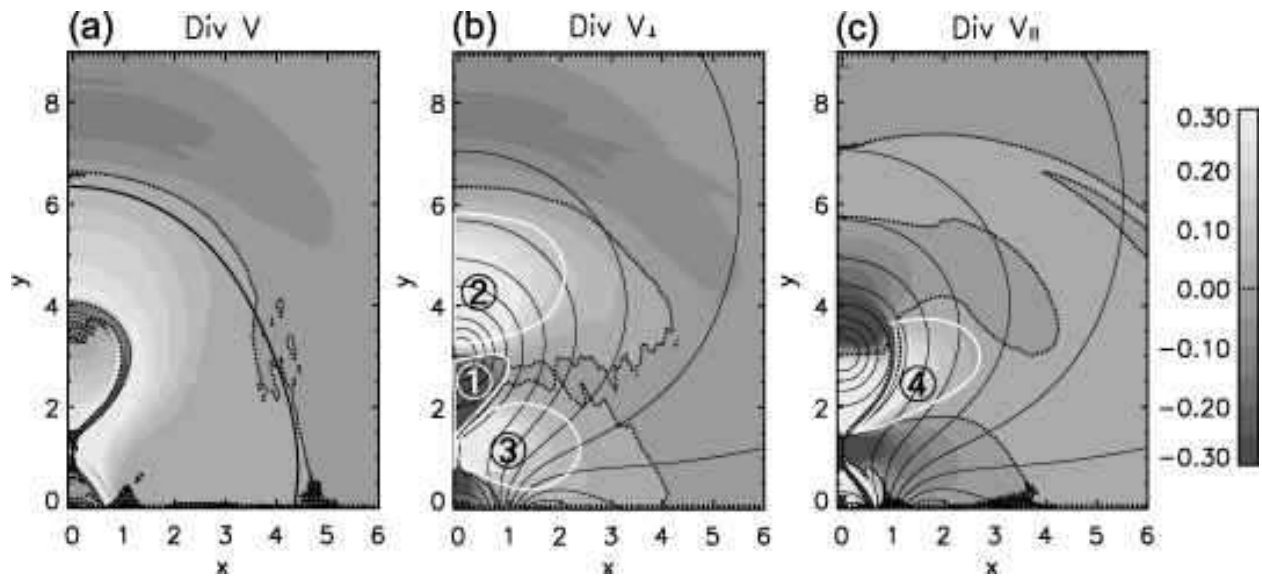


Fig. 13.— (a) Divergence of velocity at $t = 100$, and thick lines show the boundaries where plasma $\beta = 1$. (b) Divergence of velocity perpendicular to the magnetic field line. (c) Divergence of velocity parallel to the magnetic field line. Solid lines in (b) and (c) are shown magnetic field lines. Dotted lines of all panels show the boundary where the value of the divergence is equal to zero.

flux rope rises higher, the magnetic pressure inside the flux rope becomes larger than that in the ambient plasma, which leads to the expansion to the direction perpendicular to the magnetic field of the structure (region 2 displayed in Fig. 13b). This expansion is caused by the magnetic field and therefore occurs only in the region where magnetic fields are dominant. In fact, the boundary between divergence and convergence is located quite near the boundary plasma $\beta = 1$ as shown in Figure 13a. Above the region plasma $\beta < 1$, convergence is present because the plasma is swept up.

On the other hand, fast reconnection generates reconnection inflows on both sides of the reconnection region. The reconnection inflow causes the expansion of the magnetic field, and therefore the expansion of the plasma in the perpendicular direction (region 3 displayed in Fig. 13b). The expansion causes a decrease of pressure, and hence plasma flows in along the field lines. In fact, region 3 shows convergence in Figure 13c. Additionally, this converging flow causes the expansion in region 4 in Fig. 13c. Note that we can see a converged layer on the inner boundary of region 4 in Figures 13a and 13c. This corresponds to the slow shock discussed in the previous section.

These rarefaction mechanisms work simultaneously. The plasma, which flows into the reconnection region and the slow shocks, flows out partly upward and the rest flows out downward. The mass which previously existed in the rarefied regions goes partly to the CME and the the rest to the cusp-shaped loop.

4. Comparison between Simulations and Observations

We synthesized soft X-ray images from the density and temperature in the numerical results. (lower panels of Figure 3 and 4) These images were produced by taking account of the filter response function of the soft X-ray telescope (SXT) aboard *Yohkoh* (Tsuneta et al. 1991). Seen in Figure 3, the density of the reconnection outflow is very low because the temperature is very high in case A. Therefore, the high temperature regions in the flare loop are observed as cavities. Such a flare loop have never been observed in *Yohkoh* observations, while the appearance of loop in case B is consistent with observations (for example Fig. 14). The results of adiabatic case are quite different from the real corona. Therefore, we compared the results of case B with *Yohkoh*/SXT observations, in order to provide new interpretations of observed features.

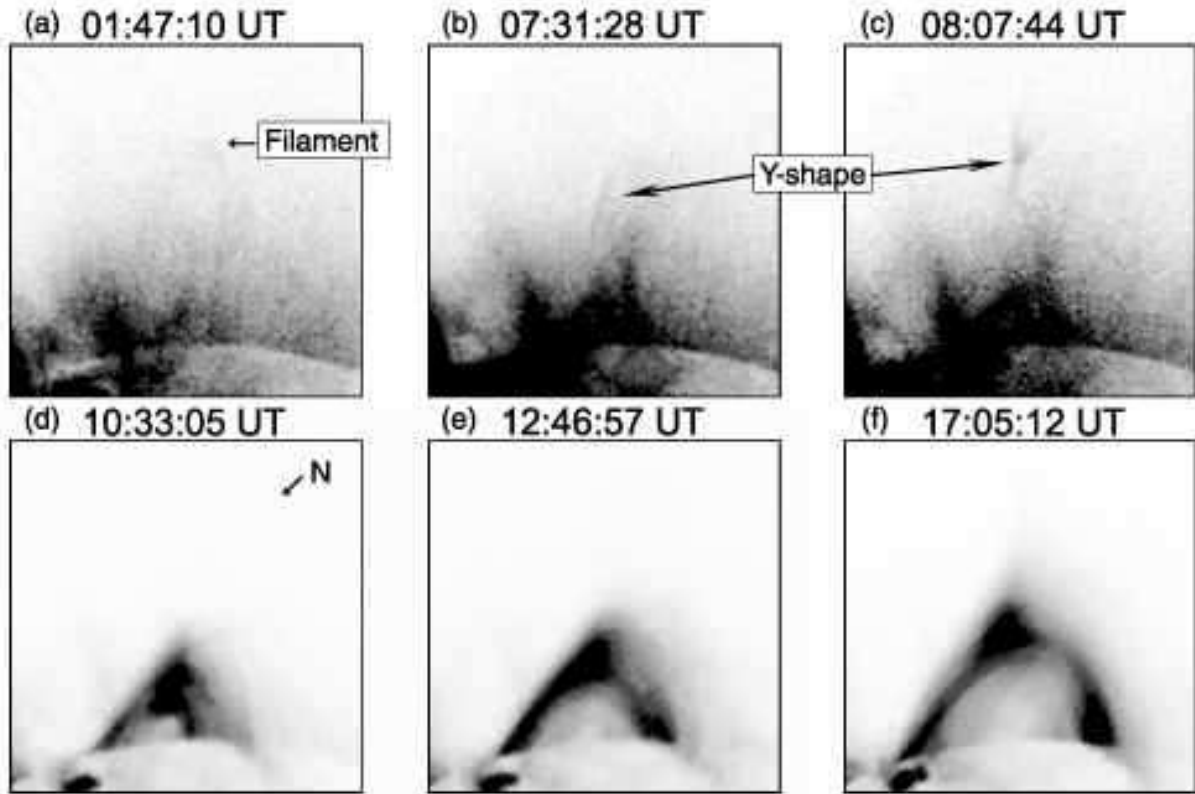


Fig. 14.— Soft X-ray images of a giant arcade on 1992 January 24, taken with Yohkoh/SXT. (a), (b), and (c) were taken with AlMg filter at half resolution ($\sim 5''$) at 01:47:10, 07:31:28, and 08:07:44 UT. A faint loop can be seen in panel (a), and it disappears before the Y-shape structure was observed. In panels (b) and (c), the Y-shaped ejecting structure was observed. (d) and (e) were taken with Al.1 filter at quarter resolution ($\sim 10''$) at 10:33:05 UT and 12:46:57 UT, respectively. (f) is taken with Al.1 filter at half resolution at 17:05:11 UT. These images are rotated with 135° to counter-clockwise, and the north direction is shown in panel (d). The spatial scale of one side of these images are 5.4×10^{10} cm.

4.1. Y-shaped Structure

Figure 14 shows the giant arcade (helmet streamer) formation on 1992 January 24 which was reported by Hiei et al. (1993). The event is thought to be face-on observation of 'giant arcade' (although it has a little orientation, see Shiota et al. 2003). In this event, after a Y-shaped structure (Fig 14b and c) is ejected, a cusp-shaped arch is formed, and then the arch seems to grow larger and larger.

These evolution in the event is consistent with our numerical results (Fig. 4). In the numerical results, after a Y-shaped structure is ejected, a cusp-shaped loop seems to grow larger and larger. Therefore, Shiota et al. (2003) suggest that the Y-shaped structure in the event may correspond to the slow and fast shocks associated with magnetic reconnection.

It is known that a slow shock associated with magnetic reconnection is dissociated into a conduction front and an isothermal slow shock in solar flares (Forbes et al. 1989; Yokoyama & Shibata 1997). On the other hand, because the temperature of arcades is not as high as that of flares, the slow shock is dissociated slightly under the condition of arcades (see Shiota et al. 2003).

4.2. Structure of Slow Shocks

What is the outer boundary of the flux rope in the numerical results? In Figures 9, the boundary is found to be a weakly current density enhanced layer, which corresponds to weak slow shocks (see §3.2). These slow shocks propagate along the field lines from the X point, along either side of the flux rope, and finally collide with each other above the flux rope. Therefore, the plasma and current densities are weakly enhanced just above the flux rope (Figure 9). After the interference, the shock waves also continue to propagate along the field lines. The flux rope continues to expand as it rises (see Fig. 11 and Fig. 13a), and the inner boundary of the expansion corresponds to the slow shocks (Figure 11). If the simulation is performed for longer time, the slow shocks will continue to propagate, producing second interference point below the flux rope. These processes will produce shell-like structures of around the flux rope (Fig. 15a). Many CMEs show their complicated structure in SOHO/LASCO observation (Cremades & Bothmer 2004, Fig. 15b). This process may explain such complicated structures of CMEs.

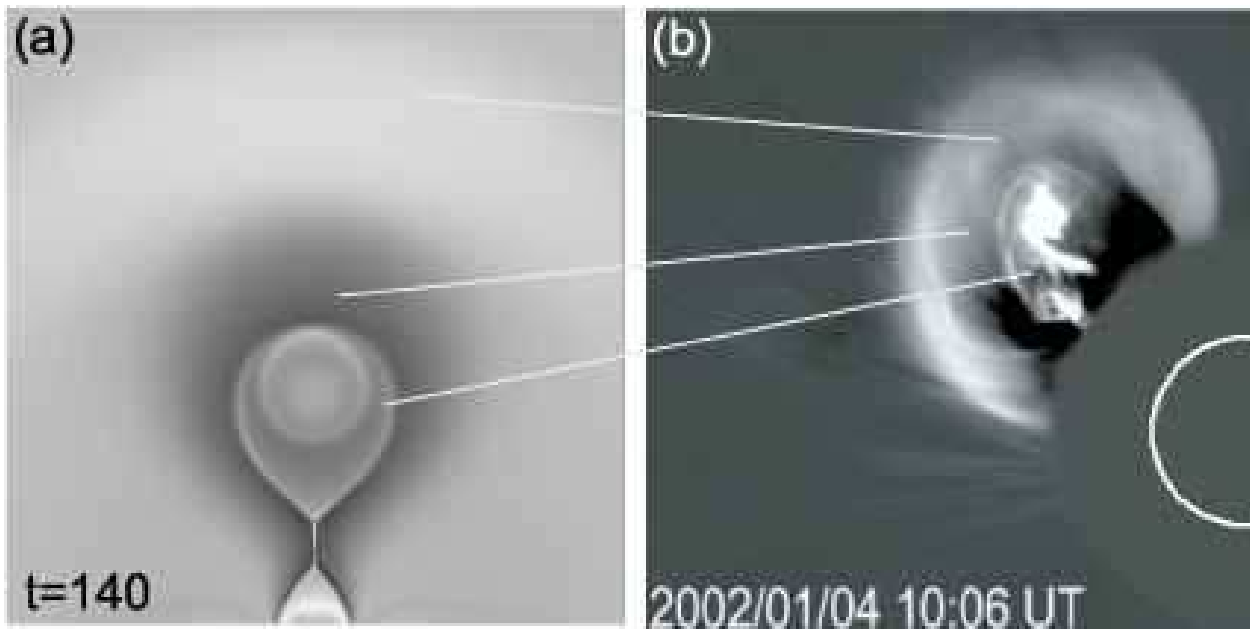


Fig. 15.— (a) density distribution at $t=140$ (b) LASCO C2 observation at 10:06 UT on January 4 2002 (Figure 15b of Cremades & Bothmer 2004)



Fig. 16.— Soft X-ray images (negative) taken with Yohkoh/SXT on 1992 January 24 and the ratio of the two images (positive). (a) and (b) were taken with Al.1 filter at half resolution at 02:55:12 UT and 14:33:53 UT, respectively. (c) is the intensity ratio of (b) to (a), and the image displays only between zero and unity.

4.3. Dimming

Recent observations reveal that solar flares often occur associated with the decrease of soft X-ray and EUV intensity, that is so-called *dimming* (Sterling & Hudson 1997; Zarro et al. 1999). Hudson (1996) showed that, also in the giant arcade on 1992 January 24, dimming occurred in the regions above the cusp-shaped arcades (shown in Fig. 16). SOHO observations indicated that the dimming is caused by the decrease in the plasma density not by the decrease in temperature (Harrison & Lyons 2000). Furthermore, Harra & Sterling (2001) showed blue-shifted motion coincided with coronal dimming in the CDS observations, and therefore, suggested the lost mass is supplied to the CME, while the mechanism has not been confirmed. Especially, the strong dimming is often observed in both sides of flare/giant arcades (Sterling & Hudson 1997; Hudson 1996), hereafter we call such strong dimming as ‘twin dimming’

We can see that the density around the flux rope and the cusp-shaped loop decreases in the simulation. The decrease in density is observed as soft X-ray dimming (Fig. 4). The dimming can be seen in both side of the X-ray arcade in the simulation, and these positions are consistent with those of twin dimming in observations. Therefore, soft X-ray twin dimming may correspond to the rarefaction in the simulation. As discussed in section 3.3, the rarefaction caused by reconnection inflow and the expansion of the flux rope. However, the expansion occurred mainly above the flux rope. Therefore the rarefaction in both side of the loop (i.e. twin dimming) are mainly caused by reconnection inflow.

4.4. Three-part Structure

From the point of view of CME structure, the numerical results provide some new interpretations. Figure 17 shows global structure seen in the results, which is very consistent with the “three part structure” observed in many CMEs. According to the numerical results, the core consists of the flux rope and slow shocks, the cavity corresponds the ‘dimming’ region around the flux rope which connected to the twin dimming regions, and the front loop corresponds to the region compressed by the forward fast shock (Fig. 17). In this results, the loop in front of the CME is very weak and not a shock, because density is not stratified owing to the absence of the gravity. In another case of our numerical result including gravity (see Shiota et al. 2004), the wave grows to a shock easily.

Lin et al. (2004) modeled a CME with semi-analytic reconnection model and explained the “three part structure” of CME as a separatrix bubble. They discussed, in the paper, that the leading edge of three-part structure corresponds to the separatrix connected to the

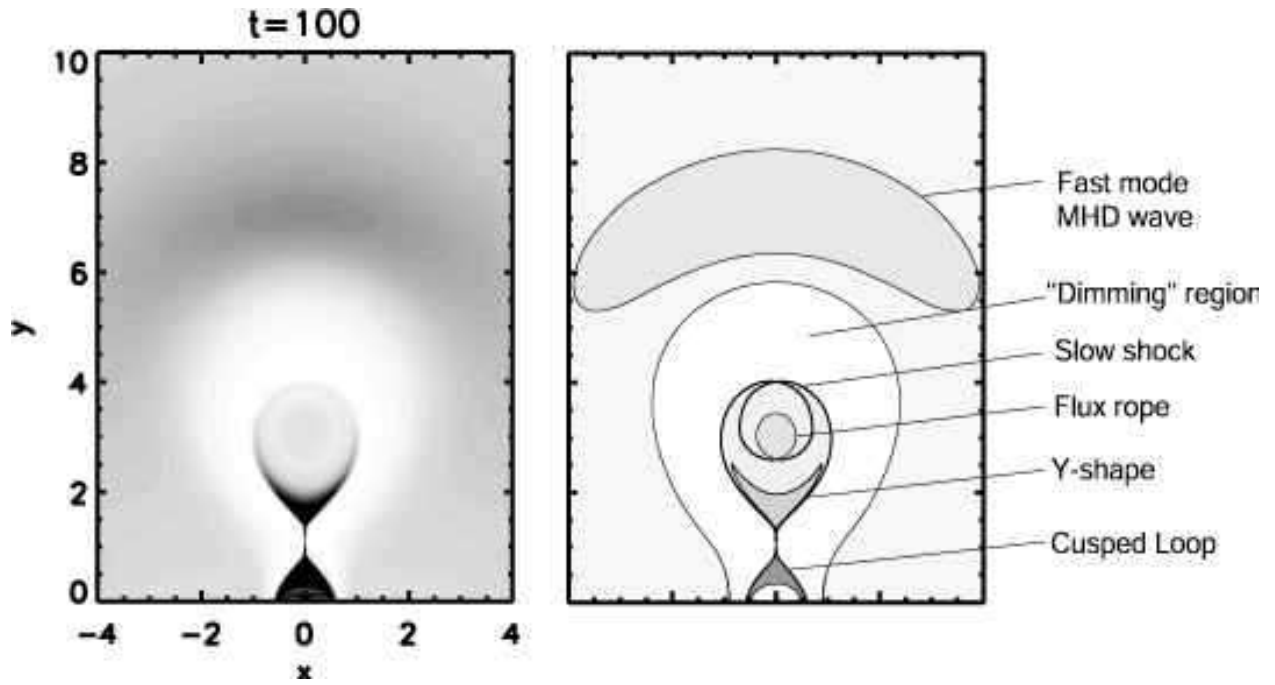


Fig. 17.— Simulated negative x-ray images. Left panel shows calculated X-ray image at $t = 100$ in case B. Right panels show simplified same image in which each features are indicated.

reconnection region. As they mentioned in the paper, their model is not realistic therefore more detailed computation is required. Our results can be applied the requirements, and suggest new interpretations (Fig. 15 and 17) successfully.

4.5. Backbone Feature of Flare Arcade

In some large arcade flares (and some giant arcades), we can see often backbone-like features, which may be a series of brighter features on the top of each loop in the arcade in soft X-ray images (Sakurai et al. 1992) while loop top bright features at the loop top are also observed in some compact flares, which are called as ‘Feldman blob’ (see Acton et al. 1992). In the event on 1992 January 24, the top of the cusp-shaped loop is brighter than other region of the loop (Figure 14d, e, and f). On the other hand, calculated X-ray images show brighter feature on the top of the cusp-shaped loops. The brighter feature is formed by the compression in the fast shock formed by the collision of the downward reconnection outflow.

In order to compare the numerical result with SXT observations more directly, we calculated 3-dimensional views of the numerical results, assuming that the numerical results distributed uniformly to the perpendicular direction. We apply the same way to calculate a 3-dimensional views as used in Forbes & Acton (1996). The calculated images are shown in Figure 18. However, the effect of gravity (density stratification) is not included in our numerical simulations. If the effect of gravity is included, the density in upper corona becomes much smaller than these results. The soft X-ray intensity is proportional to n^2 , the brightness of the feature in upper corona becomes much smaller. In fact, the center of the Y-shape is located at twice of the scale height, the intensity of the Y-shape is negligible. Therefore, we synthesized 3-dimensional soft X-ray images, in which the Y-shape is removed (the lower right two panels of Fig. 18). In the figure, the bright feature in the numerical results looks like a backbone feature. The results, hence, indicate that a backbone like feature of flare/giant arcades may correspond to the plasma compressed by the fast shock produced by a reconnection outflow.

5. CONCLUSION

In this paper, we proposed a new model that explains the formation of the three-part structure of CMEs and the mechanism of dimmings self-consistently.

we performed MHD simulations of CMEs associated with giant cusp-shaped arcades for

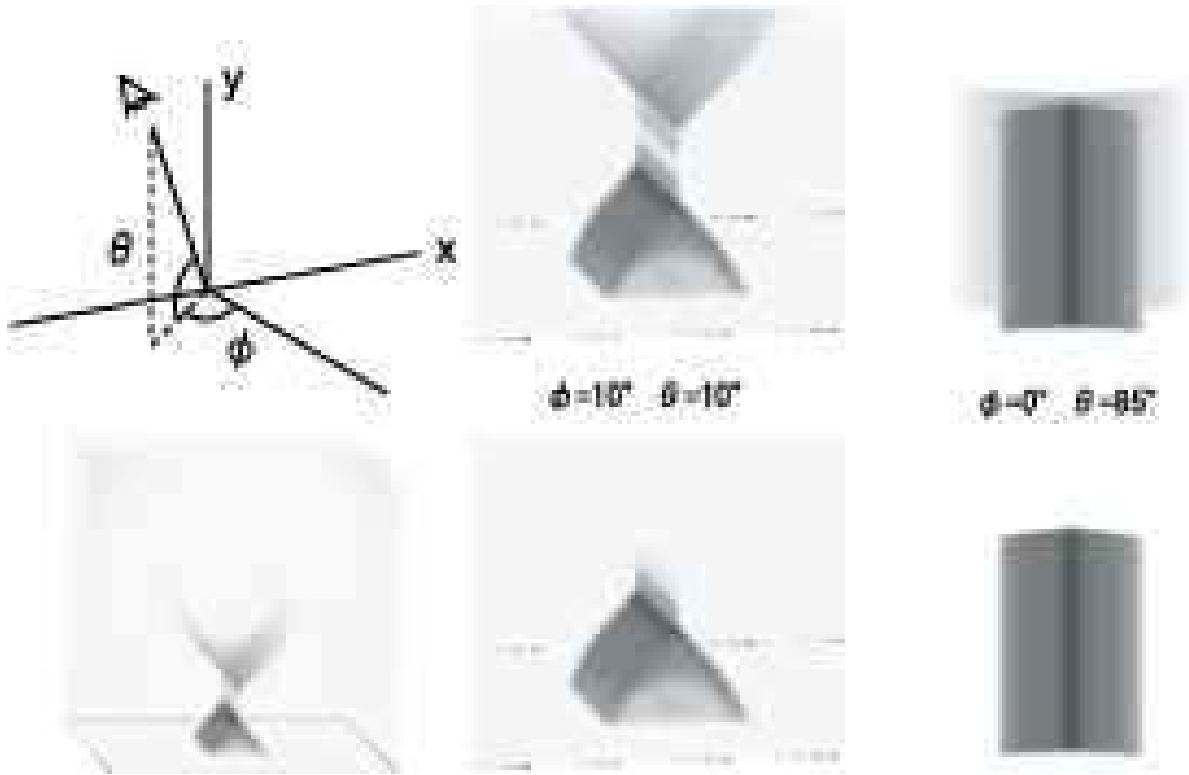


Fig. 18.— Three dimensional views of a numerical arcade at $t = 100$. The arcade is calculated with an assumption that the numerical results are uniformly arranged to the perpendicular direction. Upper panels are synthesized using numerical results with out any process. Lower panels are synthesized using data in which we remove Y-shaped ejection because such Y-shaped ejection cannot be observed in most arcade flare. Left panels are synthesized as viewed with a horizontal angle (ϕ) of 10° and with inclination angle of angle (θ) of 10° . Right panels are synthesized with a horizontal angle (ϕ) of 0° and with inclination angle of angle (θ) of 85° .

the two cases; one case includes heat conduction effect, while the other does not include. The dynamics is similar in both case, while the reconnection rate in the conductive case is enhanced slightly compared to the adiabatic case and the temperature of the loop top is consistent with the theoretical value predicted by the Yokoyama-Shibata scaling law. In the conductive case, a slow shock is hardly dissociated to an isothermal slow shock and a conduction front, different from the case for solar flares. As magnetic reconnection occurs slow and fast shocks are formed to be attached to a Y-shaped structure and a cusp-shaped loop. The slow shocks continue to propagate along the field lines around the flux rope, forming two spiral patterns. The density just outside the slow shocks decreases a great deal. This decrease in density (rarefaction) is caused by expansion and reconnection inflow simultaneously.

Compared with *Yohkoh*/SXT observations, the numerical results in case B are consistent with the observation of a giant arcade on 1992 January 24. A Y-shaped erupting structure observed in the event may correspond to the slow and fast shocks associated with the magnetic reconnection (this is reported by Shiota et al. 2003). Soft X-ray dimming is also observed in this event. The position of the dimming regions are consistent with that of the rarefaction in the numerical results. Since the rarefaction occurs in the region outside the slow shocks, the inner boundary between the “dimming” and “non-dimming” regions may be slow shocks associated with the reconnection.

The global structure in the numerical results is similar to the “three part structure” of CMEs. In the numerical results, the leading edge, cavity, and core correspond to the region compressed by piston-driven fast MHD wave, the rarefaction region, and the flux rope. The slow shocks associated with magnetic reconnection may play a role forming in complex features around the core.

According to observations the top of cusp-shaped loops in an arcade is brighter than other regions, which looks like a backbone of the arcade. Such a feature is reproduced in the numerical simulation, which indicates that the backbone feature corresponds to the fast shock created by the collision between the reconnection outflow and the arcade.

The new results of this work are as follows.

1. We found the evolution of slow shocks associated with reconnection in the configuration initially a flux rope exits. The numerical results indicate that complex structures around a CME core may be formed by these slow shocks.
2. We proposed a self-consistent model of ‘dimming’. The decrease in density observed as ‘dimming’ is caused by expansion and reconnection inflow simultaneously. In the numerical results, the cavity of the three-part CME is connected to the ‘dimming’ regions, and therefore

the density decrease mechanisms are the same. We proposed a new interpretation of three-part structure of CMEs (Fig. 17).

3. The backbone-like features observed in many flare/giant arcades can be explained as the fast shock created by the collision between the reconnection outflow and the arcade.

The authors thank D. H. Brooks, J. Lin, T. Miyagoshi, A. Asai, H. Tonooka, and T. Yokoyama, for useful discussions. The Yohkoh satellite is a Japanese national project, launched and operated by ISAS, involving many domestic institutions, and with international collaboration of US and UK. D. S. is supported by Research Fellowship of the Japan Society for the Promotion of Science (JSPS) for Young Scientist. The visit of P. F. C. to Kyoto University was supported by the JSPS. P. F. C. is supported by NSFC (10333040 and 10403003). This work is supported by the Grant-in-Aid for the 21st Century COE "Center for Diversity and Universality in Physics" from the Ministry of Education, Culture, Sports, Science and Technology (MEXT) of Japan. This work was partly supported by the Grants-in Aid of the MEXT of Japan (16340058, KS). This work was supported in part by the JSPS Japan-UK Cooperation Science Program (principal investigators: K. Shibata and N. O. Weiss).

REFERENCES

- Acton et al. 1992, 1992, PASJ, 44, L71
- Chen, P. F., Fang, C., Ding, M. D., & Tang, Y. H. 1999, ApJ, 520, 853
- Chen, P. F., & Shibata, K. 2000, ApJ, 545, 524
- Coppi, B., & Friedland, A. B. 1971, ApJ, 169, 379
- Cremades, H. & Bothmer, V., 2004, Astron. Astrophys., 422, 307
- Feynman, J. & Martin, S. F., 1995, J. Geophys. Res., 100, 3355
- Forbes, T. G., & Acton, L. W., 1996, ApJ, 459, 330
- Forbes, T. G., & Lin, J., 2000, J. Atmos. Sol.-Terr. Phys., 62, 1499
- Forbes, T. G., Malherbe, J. M., & Priest, E. R. 1989, Sol. Phys., 120, 285
- Hanaoka, Y., et al. 1994, PASJ, 46, 205

- Harra, L. K. & Sterling, A. C. 2001, *ApJ*, 561, L215
- Harrison, R. A., & Lyons, M. 2000, *Astron. Astrophys.*, 358, 1097
- Hiei, E., Hundhausen, A. J., & Sime, D. G. 1993, *Geophys. Res. Lett.*, 20, 2785
- Hirayama, T. 1974, *Sol. Phys.*, 34, 323
- Hu, Y. Q. 1989, *J. Comput. Phys.*, 84, 441
- Hudson, H. S. 1996, in *IAU Colloq. 153 Magnetodynamic Phenomena in the Solar Atmosphere - Prototypes of Stellar Activity*, ed. Y. Uchida, T. Kosugi, & H. S. Hudson (Dordrecht: Kluwer), 89
- Hundhausen, A. 1999, *the many faces of the sun : a summary of the results from NASA's Solar Maximum Mission*. ed. by Keith T. Strong, Julia L. R. Saba, Bernhard M. Haisch, and Joan T. Schmelz. (New York: Springer), p.143
- Illing, R. M. E. & Hundhausen, A. J. 1985, *J. Geophys. Res.*, 90, 275
- Kahler, S. W. 1992, *Annu. Rev. Astron. Astrophys.*, 30, 113
- Lin, J., Forbes, T. G., & Isenberg, 2001, *J. Geophys. Res.*, 106, 25053
- Lin, J., Raymond, J. C., & van Ballegoijen, A. A., 2004, *ApJ*, 602, 422
- McAllister, A. H., Dryer, M., McIntosh, P., Singer, H., & Weiss, L. 1996, *J. Geophys. Res.*, 101, 13497
- Magara, T., Mineshige, S., Yokoyama, T., & Shibata, K., 1996, *ApJ*, 466, 1054
- Munro, R. H., Gosling, J. T., Hildner, E., MacQueen, R. M., Poland, A. I., & Ross, C. L., 1979, *Sol. Phys.*, 61, 201
- Nitta, S., Tanuma, S., Shibata, K., & Maezawa, K. 2001, *ApJ*, 550, 1119
- Priest, E. R. 1982 *Solar Magnetohydrodynamics* (Dordrecht: Reidel), chap. 5.4
- Raymond, J. C., Cox, D. P., & Smith B. W. 1976, *ApJ*, 204, 290
- Sakurai, T., Shibata, K., Ichimoto, K., Tsuneta, S., & Acton, L. W. 1992, *PASJ*, 44, L123
- Sato, T., Hayashi, T., Watanabe, K., Horiushi, R., Tanaka, M., Swairi, N., & Kusana, K., 1992, *Phis. Fluids B*, 4, 450

- Shibata, K., Masuda, S., Shimojo, M., Hara, H., Yokoyama, T., Tanuma, S., Kosugi, T., & Ogawara, Y. 1995, *ApJ*, 451, L83
- Shibata, K., 1996, *Adv. Space Res.*, 17, 9
- Shibata, K., 1999, *Astrophys. Sp. Sci.*, 264, 129
- Shiota, D. et al. 2003, *PASJ*, 55, L35
- Shiota, D. et al. 2004, in *ASP Conf. Ser. 325, The Solar-B Mission and the Forefront of Solar Physics -Proceeding of the Fifth Solar-B Science Meeting-*, ed. T. Sakurai & T. Sekii (San Francisco: ASP), 373
- Spitzer, L., Jr. 1962 *Physics of Fully ionized Gases*, Interscience Pub., New York, Chap. 5
- Sterling, A. C. & Hudson, H. S. 1997, *ApJ*, 491, L55
- Tsuneta, S., et al. 1991, *Sol. Phys.*, 136, 37
- Tsuneta, S., Takahashi, T., Acton, L. W., Bruner, M. E., Harvey, K. L., & Ogawara, Y. 1992, *PASJ*, 44, L211
- Tsuneta, S. 1996, *ApJ*, 456, 840
- Ugai, M. & Tsuda, T. 1977, *Journal of Pla. Phys.*, 17, 337
- Webb, D. F. & Hundhausen, A. J. *Sol. Phys.*, 1987, 108, 383
- Yamamoto, T. T., Shiota, D., Sakajiri, T., Akiyama, S., Isobe, H., & Shibata, K. 2002, *ApJ*, 579, L45
- Yokoyama, T., & Shibata, K. 1997, *ApJ*, 474, L61
- Yokoyama, T., & Shibata, K. 1998, *ApJ*, 494, L113
- Yokoyama, T., & Shibata, K. 2001, *ApJ*, 549, 1160
- Zarro, D. M., Sterling, A. C., Thompson, B. J., Hudson, H. S., & Nitta, N. *ApJ*, 1999, 520, L139